This manuscript has been authored by UT-Battelle, LLC under Contract No. DE-AC05-00OR22725 with the U.S. Department of Energy. The United States Government retains and the publisher, by accepting the article for publication, acknowledges that the United States Government retains a non-exclusive, paid-up, irrevocable, world-wide license to publish or reproduce the published form of this manuscript, or allow others to do so, for United States Government purposes. The Department of Energy will provide public access to these results of federally sponsored research in accordance with the DOE Public Access Plan(http://energy.gov/downloads/doe-public-access-plan).

Toho-1 β-Lactamase: Backbone Chemical Shift Assignments and Changes in Dynamics upon Binding with Avibactam

Varun V. Sakhrani,[a] Rittik K. Ghosh,[b] Eduardo Hilario,[a] Kevin L. Weiss,[c] Leighton Coates,[d,*] and Leonard J. Mueller[a,*]

[a]Department of Chemistry, University of California Riverside, Riverside, CA 92521, USA

[b]Department of Biochemistry, University of California Riverside, Riverside, CA 92521, USA

[c]Neutron Scattering Division, Oak Ridge National Laboratory, 1 Bethel Valley Road, Oak Ridge, TN, 37831, USA

[d]Second Target Station, Oak Ridge National Laboratory, 1 Bethel Valley Road, Oak Ridge, TN, 37831, USA

*Corresponding Authors: leonard.mueller@ucr.edu, ORCID: 0000-0002-2607-9875, coatesl@ornl.gov, ORCID 0000-0003-2342-049X

Abstract

Backbone chemical shift assignments for the Toho-1 β-lactamase (263 amino acids, 28.9 kDa) are reported based on triple resonance solution-state NMR experiments performed on a uniformly ^{2}H,^{13}C,^{15}N-labeled sample. These assignments allow for subsequent site-specific chemical, structural, and dynamical characterization. At the chemical level, titration with the non-β-lactam β-lactamase inhibitor avibactam is found to give chemical shift perturbations indicative of tight covalent binding that allow for mapping of the inhibitor binding site. At the structural level, protein secondary structure is predicted based on the backbone chemical shifts and protein residue sequence using TALOS-N and found to agree well with structural characterization from X-ray crystallography. At the dynamical level, model-free analysis of ^{15}N relaxation data at an initial, single field of 16.4 T reveals well-ordered structures for the ligand-free and avibactam-bound enzymes with generalized order parameters of ~0.85. Complementary relaxation dispersion experiments indicate that upon substrate binding, there is an escalation in motions on the millisecond timescale in the vicinity of the active site. The combination of high rigidity on short timescales and active site flexibility on longer timescales is consistent with hypotheses for achieving both high catalytic efficiency and broad substrate specificity: the induced active site dynamics allows variously sized substrates to be accommodated and increases the probability that the optimal conformation for catalysis will be sampled.

Abbreviations: HSQC, heteronuclear single quantum coherence; NMR, nuclear magnetic resonance; RMSD, root mean square deviation; RCI, random coil index

Keywords: β-lactamase, protein NMR, backbone chemical shift assignments, avibactam, non-β-lactam inhibitors, ^{15}N backbone amide relaxation, protein backbone dynamics, ligand-protein binding

INTRODUCTION

β-lactam antibiotics inhibit the synthesis of bacterial cell walls by targeting penicillin-binding proteins (PBPs). The binding of β-lactam antibiotics to PBPs makes them chemically inert, leading to bacterial cell death. β-lactam antibiotics remain the most widely used in antimicrobial chemotherapy due to their low toxicity, as there are no human counterparts of their bacterial targets (Kong et al. 2010). To counter these potent antimicrobials, bacteria have evolved to produce β-lactamase enzymes that cleave the amide bond within the β-lactam ring via a general base hydrolysis mechanism (Bebrone et al. 2010; Bush 2010). This family of hydrolytic enzymes can be divided into four distinct classes based on sequence homology, with classes A, C, and D utilizing a catalytic serine residue to hydrolyze the β-lactam ring, while class B are metalloenzymes that utilize active-site zinc ion(s) to perform the hydrolysis (Bush 2013). Representative families of class A β-lactamases are TEM, SHV, and the class A extended-spectrum β-lactamases (ESBL) CTX-M (Jacoby 2006); the latter includes the Toho-1 β-lactamase studied here (also classified as CTX-M-44). ESBLs were found in the 1980s and exhibit increased hydrolytic activity against first, second, and third generation extended-spectrum cephalosporins and monobactam antibiotics.

Along with the development of β-lactamase-resistant antibiotics, the strategy towards combatting resistance includes combining β-lactam antibiotics with mechanism-based β-lactamase inhibitors (Tooke et al. 2019). Clavulanic acid, sulbactam, and tazobactam are examples of β-lactam-based inhibitors active against class A β-lactamases that were introduced into clinical practice four decades ago (Drawz and Bonomo 2010). These inhibitors form a stable acyl-enzyme intermediate with the catalytic serine (S70), but eventually the bound inhibitor hydrolytically deacetylates and regenerates the catalytically active enzyme (Helfand et al. 2003).

The increasing abundance of ESBL-producing pathogens has driven increased use of and reliance on carbapenems, a class of highly effective antibiotic agents reserved for the treatment of severe or high-risk bacterial infections (Shirley 2018). The emergence and spread of carbapenemase-producing pathogens are particularly concerning and have highlighted the urgent need for new antimicrobial agents. Classical β-lactamase inhibitors such as clavulanic acid, tazobactam, and sulbactam lack activity against many classes of β-lactamases, meaning that many first-generation β-lactam/β-lactamase inhibitor combinations are frequently ineffective against multidrug-resistant pathogens (Shirley 2018).

The emergence of resistant class A β-lactamases (Bebrone et al. 2010) continues to motivate the development of novel inhibitors that are capable of impeding antibiotic resistance by being structurally different from β-lactam ring containing substrates. Avibactam, a member of the class of azabicycloalkanes, is one such non-β-lactam β-lactamase inhibitor that is approved by the FDA as part of combination therapies for the treatment of complicated intra-abdominal and urinary tract infections (Lagacé-Wiens et al. 2014). Ceftazidime-avibactam, sold under several brand names, is an intravenously administered combination of the third-generation cephalosporin ceftazidime and avibactam. It has excellent in vitro activity against many Gram-negative pathogens, including many ESBLs. However, it is not active against metallo-β-lactamase (Class B) producing bacterial strains (Shirley 2018).

Avibactam does not have a β-lactam core, and a sulfate moiety replaces the carboxyl group, as shown in Fig. 1. Avibactam forms a unique carbamyl covalent linkage with the catalytic serine, which does not hydrolytically dissociate. Instead, the decarbamylation leads to the recyclization of the azabicyclooctane ring structure, reforming the intact inhibitor capable of further inhibition (Ehmann et al. 2012).

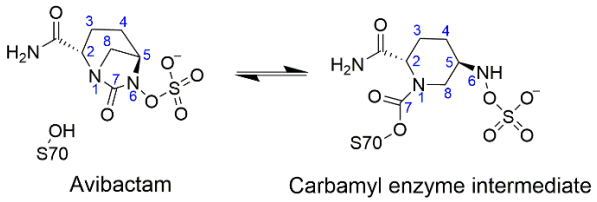

Fig. 1 The reversible avibactam-mediated inhibition of class A β-lactamases. During the inhibition reaction, the N6-C7 bond is broken, and N6 is protonated, resulting in the opening of the diazobicyclooctane (Langan et al. 2020)

Previous kinetic, mutagenesis, spectroscopic, and computational studies have tried to elucidate the molecular details related to the activation of the catalytic serine residue during catalysis (Damblon et al. 1996; Tomanicek et al. 2013; Langan et al. 2016; Vandavasi et al. 2016; Langan et al. 2018) and during inhibition by avibactam (Ehmann et al. 2012; Lahiri et al. 2013; King et al. 2016; Lizana and Delgado 2018; Pemberton et al. 2020). There is still considerable debate over the exact roles of the active site lysine (K73), serine (S130), and glutamic acid (E166) residues, as well as the active site water molecule.

The dynamical properties of β-lactamases are linked to their biological function and are thought to play an essential role in governing the evolution of this family of enzymes (Petrovic et al. 2018). Recent computational modeling studies have addressed the role of dynamics towards conferring resistance in the evolution of Class-A β-lactamases (Verma et al. 2013; Zou et al. 2015; Cortina and Kasson 2016; Hart et al. 2016). These studies concentrate primarily on sequence comparisons, but it appears that sequence and structure alone are not enough to classify the physicochemical properties across the class-A β-lactamases: detailed comparisons of electrostatic and dynamical properties are necessary to reflect evolutionary trends. This highlights the need for empirical data on dynamics for modern class-A members (Verma et al. 2013). To date, the dynamics of a small number of class-A β-lactamases including TEM-1, PSE-4, and BlaC have been characterized by NMR relaxation experiments to obtain residue-specific generalized order parameters and local correlation times (Savard and Gagné 2006; Morin and Gagné 2009; Fisette et al. 2010; Fisette et al. 2012; Elings et al. 2020). These experiments show well-ordered structures, with generalized order parameters on the picosecond-to-nanosecond timescale of ~ 0.85-0.9, with microsecond-to-millisecond motions in the vicinity of the active site. This combination of high rigidity on short timescales and active site flexibility on longer timescales is consistent with hypotheses for achieving both high catalytic efficiency and broad substrate specificity (Fisette et al. 2010).

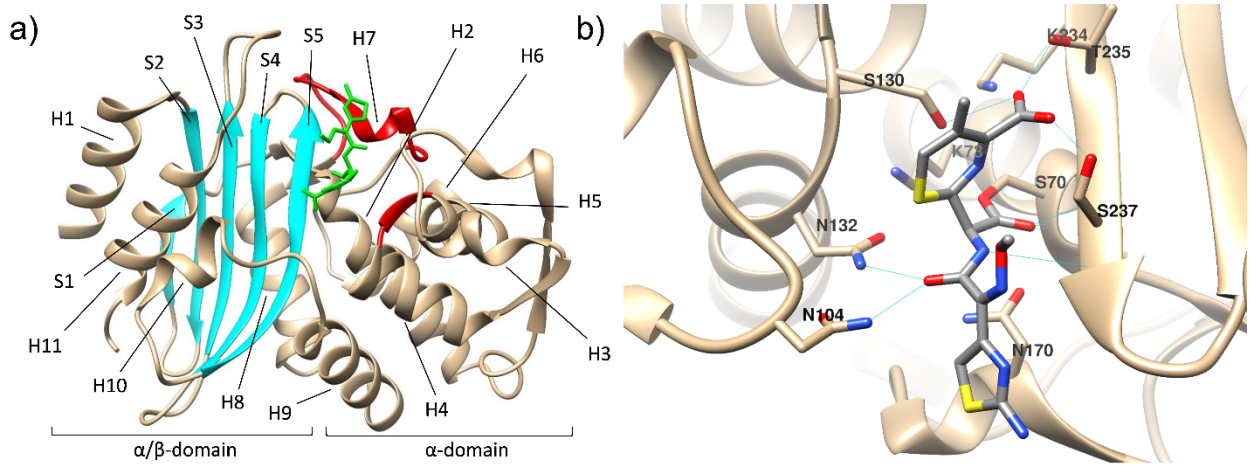

Fig. 2 (a) Ribbon model of the Toho-1 β-lactamase from X-ray crystallography (PDB ID: 1IYO) (Shimamura et al. 2002). The β-strands forming the β-sheet in the alpha-beta domain are shown in blue. The Ω loop and SDN loop are shown in red. The antibiotic cefotaxime is shown in green bound in the active site. (b) The active site highlighting sidechains that interact with cefotaxime; blue lines indicate hydrogen bonds. Catalytic residue E166, mutated to A166 in this structure, is not shown. Figure prepared using Chimera (Pettersen et al. 2004)

Here we examine the dynamics of the Toho-1 β-lactamase in the absence and presence of the non-β-lactam β-lactamase inhibitor avibactam. Based on sequence homology and activity against extended-spectrum cephalosporins, Toho-1 β-lactamase is classified as a CTX-M-type extended-spectrum β-lactamase (ESBL) (Ishii et al. 1995). This modern member of the class A enzymes is a 263-residue protein and consists of two highly conserved domains (α/β and α) with the active site cavity formed at their interface (Fig 2). Helix H2 forms the active site's base/bottom and provides the catalytic residues S70 and K73. Three structural motifs lying over the base form a cavity for the active site. The first of these is the segment consisting of residues S130, D131, and N132 (SDN loop), between helices H4 and H5, of which S130 is the catalytic residue. Strand S5 provides catalytic residues K234 and T235 and forms the second structural motif. The third motif consists of the N-terminal portion of the Ω loop and provides the catalytic residue E166. The 16 residue-long Ω loop (consisting of residues 164 to179 and devoid of any extended secondary structure other than helix H7) and the 9 residue-long SDN loop are standard, defining features of class A β-lactamases. The presence of a network of hydrogen bonds and salt bridges between the catalytic residue sidechains rigidifies the active site in the absence of a substrate, as seen in the crystal structure of the free enzyme (PDB ID: 2ZQ8) (Shimamura et al. 2009).

Within the Ω loop of class A β-lactamases members, the backbone amide and side chain of R164 form salt bridges to the side chain of D179 to maintain a "bottleneck" structure having mobility essential for substrate recognition and catalysis (Banerjee et al. 1998). Reduced Ω loop flexibility correlates with increased hydrolysis of antibiotic cefotaxime (Hart et al. 2016). The loop contains the active site residue El66, which is highly conserved in class A β-lactamases and has been shown to participate in the deacylation and acylation steps of the catalytic cycle via a water molecule, potentially competing with K73 (Lobkovsky et al. 1993; Langan et al. 2020). Mutations within the Ω loop affect catalytic specificity and mechanism and play a role in governing the evolution of this class of enzymes (Petrosino and Palzkill 1996; Stojanoski et al. 2015; Patel et al. 2017). In contrast to the other ESBL's, the Ω loop in Toho-1 β-lactamase is shifted to (rests on) helix H5 instead of H6, which avoids steric interactions with the bulky side chain of oxyimino-cephalosporins, resulting in improved affinities for these substrates (Shimamura et al. 2002).

Complexes of the wild-type β-lactamases with their target substrates such as cefotaxime cannot typically be characterized by solution-state NMR because of the rapid turnover rate (the crystal structure shown in Fig. 2 is for the E166A mutant, which is unable to hydrolyze the substrate). Inhibitors such as avibactam, however, remain covalently bound for the duration of the experiment (Elings et al. 2020). Here, we make use of this extended stability to

characterize both the Toho-1 β-lactamase free in solution and in complex with avibactam. Backbone chemical shift assignments are reported for the R274N/R276N double mutant of Toho-1 β-lactamase based on triple resonance solution-state NMR experiments on a uniformly ^{2}H,^{13}C,^{15}N-labeled sample. The non-active-site R274N/R276N mutations prevent the protein's aggregation in solution. Based on these assignments and the protein sequence, the secondary structure is predicted. Perturbations in the assigned chemical shifts upon titration with avibactam allows for mapping of the inhibitor binding site. ^{15}N relaxation data obtained for ^{2}H,^{15}N-labeled samples at a single field are analyzed by model-free analysis (MFA) to obtain residue-specific dynamical parameters, including the generalized order parameter (S^2), local correlation time (τ_e), and residual exchange contribution (R_{ex}). Complementary relaxation dispersion experiments indicate that binding of the inhibitor avibactam leads to enhanced dynamics on the millisecond timescale in and around the active site. The combination of high rigidity on short timescales and active site flexibility on longer timescales is proposed to play an important role in effecting both high catalytic efficiency and broad substrate specificity.

EXPERIMENTAL

Expression and Purification of Recombinant Protein:

Uniformly ^{2}H-^{15}N labeled and ^{2}H-^{13}C-^{15}N labeled Toho-1 β-lactamase were expressed and purified as described previously with some modifications (Tomanicek et al. 2010; Langan et al. 2016). Briefly, BL21 *E. coli* cells harboring the Toho-1 β-lactamase expression plasmid were cultured and progressively adapted to $^{2}H_2O$ in minimal medium containing D-glucose in a shaking incubator set to 250 rpm and 303 K. Once adapted to $^{2}H_2O$, the cells were transferred to a modified $^{2}H_2O$ minimal medium containing 5.4 g/l ^{2}H-^{13}C-D-glucose (Cambridge Isotope Labs) 2 g/l $^{15}NH_4SO_4$ (Sigma Aldrich), 15.8 g/L Na_2HPO_4, and 4.8 g/l KH_2PO_4. After growth in the triple-labeled medium, the culture was scaled up to 500 ml split equally between two 2.8 l baffled Fernbach flasks for sufficient aeration. After the culture reached OD_{600}~1.9, IPTG was added to 0.5 mM. After 6 hours of induction, the cells were harvested by centrifugation, and the pellets were stored at 193 K until further use. For purification, the frozen cells were thawed and resuspended in lysis buffer (50 mM MES pH 6.5, 1 mM EDTA) containing SigmaFast™ EDTA-free protease inhibitor cocktail tablets (Sigma Aldrich). The cells were then lysed on ice by sonication with a Branson 450D Digital Sonifier (Emerson Industrial Automation, St. Louis, MO, USA) and clarified by centrifugation at 34000 x g for 45 min at 277 K. Following centrifugation, the supernatant was filtered through 1.6 µm and 0.45 µm GD/X syringe filters (GE Healthcare, Pittsburgh, PA, USA) as well as diluted with 20 mM MES, pH 6.5 buffer. The crude protein solution was then loaded onto a 5 ml HiTrap SP Sepharose FF column (GE Healthcare) that had been previously equilibrated with Buffer A (20 mM MES, pH 6.5). A linear gradient of Buffer B (20 mM MES, 300 mM NaCl pH 6.5) was used to elute the protein at approximately 20-30 mM NaCl at room temperature. Using UV absorbance measurements and SDS-PAGE analysis, fractions containing pure protein were selected, pooled, and concentrated using a 10 K MWCO Vivaspin 15R concentrator (Sartorius, Gottingen, Germany). Concentrated protein was loaded onto a 120-ml HiPrep Sephacryl S-100 HR gel filtration column (GE Healthcare) pre-equilibrated with Buffer A. Using UV absorbance and SDS-PAGE analysis, fractions containing pure protein were again selected, pooled, and concentrated using a 10 K MWCO Vivaspin 15R concentrator (Sartorius). The protein concentration was estimated using UV absorbance.

Backbone Sequential Assignments and Secondary Structure Predictions

Backbone chemical shift assignments for the uniformly ^{2}H-^{13}C-^{15}N labeled Toho-1 β-lactamase in the absence and presence of avibactam (at 1.2 times the protein concentration) were obtained using TROSY-based ^{1}H-^{15}N HSQC and triple resonance HNCACB/HN(CO)CACB and HNCO/HN(CA)CO experiments (Riek et al. 2000; Fernández and Wider 2003; Cavanagh et al. 2007). The protein concentration of the sample was approximately 800-850 µM in pH 6.5, 20 mM MES buffer, containing 1 mM DTT, 1 mM Na_2EDTA, 0.05% NaN_3, and 10% (v/v) $^{2}H_2O$. Data were acquired at 298 K on a Bruker AVANCE III spectrometer operating at 16.44 T (700.23 MHz ^{1}H) with a cryogenically cooled probe equipped with Z-axis pulsed field gradients. All experiments were conducted with 8 scans per indirect dimension time point, and an interscan delay of 1 s. 2D experiments took about 40 minutes, whereas each 3D experiment took 1-2 days. Detailed acquisition parameters for the NMR experiments are summarized in Table S1 (ESM).

Spectra were processed using Bruker TopSpin version 3.6. Backbone pre-assignments were carried out using synchronous inspection and strip comparisons of NH planes in NMRFAM-SPARKY (Lee et al. 2015). Automated peak picking and probabilistic assignments were carried out using APES (Shin et al. 2006), implemented in NMRFAM-SPARKY, and the PINE algorithm, implemented on the I-PINE webserver (Bahrami et al. 2009; Lee et al. 2019) and accessed via the PINE-SPARKY.2 plug-in (Lee and Markley 2018). Backbone torsion angle constraints and secondary structure prediction were derived by TALOS-N (Shen and Bax 2013). Referencing errors and chemical shift outliers were detected using the linear analysis of chemical shifts (LACS) algorithm (Wang et al. 2005), and then used to recalibrate the chemical shift scales that were initially referenced to an internal standard of 4,4-dimethyl-4-silapentane-1-sulfonic acid (DSS) (Shimizu et al. 1994).

NMR Relaxation Experiments

^{15}N-backbone amide longitudinal relaxation rates (^{15}N-R_1) and in-phase transverse relaxation rates (^{15}N-R_2) of the isolated and inhibitor-bound ([inhibitor]/[protein]=1.2) Toho-1 β-lactamase were measured on the uniformly ^{2}H-^{15}N labeled protein at 700 MHz (^{1}H) and 25 ºC using gradient-enhanced phase-sensitive HSQC pulse sequences containing a water flip-back pulse. Delays of 20, 60, 100, 200, 400, 600, 800, and 1200 ms were used for ^{15}N-R_1 experiments, and Carr-Purcell-Maiboom-Gill (CPMG) loop lengths of 16, 32, 64, 128, 160, 192, 224, and 256 ms were used for ^{15}N-R_2 measurements. Within the interleaved CPMG loop, the delay between the ^{15}N 180º pulses was 900 µs, and the ^{15}N pulse width was 100 µs. The ^{15}N-R_1 and ^{15}N-R_2 experiments were conducted with 8 transients per increment and an interscan delay of 2 s and 1 s, respectively. Additional acquisition parameters are provided in Table S1. Best-fit relaxation rates were calculated by non-linear least-squares fitting of ^{15}N-^{1}H cross-peak intensities to a two-parameter single-exponential decay in NMRFAM-SPARKY.

{^{1}H}-^{15}N steady-state NOEs were obtained by measuring the percent change in intensity for spectra obtained with and without ^{1}H pre-saturation. Saturation was obtained by applying cycles consisting of a 120º pulse (pulse width 14.2 µs) followed by a 5 ms delay during the 10 s recycle (relaxation) delay. The spectral widths were identical to those for ^{15}N-R_1 and R_2 experiments, and all relaxation experiments were performed with interleaved acquisition.

CPMG relaxation dispersion experiments were performed as detailed by Tollinger (Tollinger et al. 2001), with blocks of ^{15}N 180° pulses resulting in effective fields of frequencies (υ_{CPMG}) of 25, 50, 100, 250, 500, 750, and 1000 s^{-1} in a 40-ms constant time echo period. The carrier was set at 117 ppm and data were acquired in an interleaved manner with a recycle delay of 2 s. Effective transverse relaxation rates (R_2') were calculated from the peak heights measured at the end of the constant CPMG period, and R_{ex} was calculated as the difference between R_2' at υ_{CPMG} = 25 s^{-1} and R_2' at υ_{CPMG} = 1,000 s^{-1}. Uncertainty in R_2' was calculated based on the noise measured in a reference spectrum acquired with no CPMG block (Ishima and Torchia 2005).

Model-Free Analysis and Model Selection

^{15}N relaxation data were analyzed as described and implemented in a series of integrated Mathematica notebooks by Spyracopoulos (Spyracopoulos 2006). The workflow included calculation of the moment of inertia tensor from structural coordinates, alignment of an effective, axially symmetric rotational diffusion tensor, and model-free analysis of ^{15}N-R_1, R_2, and {^{1}H}-^{15}N NOE data with model selection of the relaxation data. The workflow is summarized below.

To begin, the relative principal components of the inertia tensor of Toho-1 β-lactamase were calculated from the X-ray crystal structure of the free enzyme (PDB ID: 2ZQ8) (Shimamura et al. 2009) and determined to be 1.00, 0.88, and 0.59. The anisotropic rotational diffusion tensor was therefore modeled as axially symmetric, and the principal components and orientation were obtained by non-linear numerical optimization using the per residue values of backbone ^{15}N T_1/T_2 relaxation ratio (using model 1 below and a fixed order parameter of 0.85) and the atomic coordinates (Tjandra et al. 1995), with more dynamic residues (i.e., having {^{1}H}–^{15}N NOE values below a cutoff value of 0.65 or significantly decreased ^{15}N T_2 values) excluded from the analysis. The results did not change appreciably when the assumed fixed order parameter was increased to 0.9. Constraints for the perpendicular ($D_x = D_y = D_\perp$) and parallel ($D_z = D_\parallel$) components of the rotational diffusion tensor with respect to the unique axis, required for optimization, were estimated using the program HYDROPRO with the hydrodynamic radius of the elements

(parameter a) set to 2.9 Å (Ortega et al. 2011). The non-linearly optimized principal components for the free protein were determined to be $D_x = D_y = D_\perp = 1.19153 \times 10^7$ s^{-1} and $D_z = D_\parallel = 1.63807 \times 10^7$ s^{-1}, which gave an effective rotation correlation time, $1/(2D_\parallel + 4D_\perp)$, of 12.43 ns and an anisotropy, $D_\parallel/D_\perp$, of 1.375 (Woessner 1962). The principal components for the avibactam-bound form were determined separately to be $D_x = D_y = D_\perp = 1.215 \times 10^7$ s^{-1} and $D_z = D_\parallel = 1.530 \times 10^7$ s^{-1}, giving an anisotropy of 1.26 and an effective rotation correlation time of 12.39 ns.

The principal components ($D_\perp$, $D_\parallel$) and orientation of the rotational diffusion tensor were used for performing standard local model-free analysis (MFA) of ^{15}N-R_1, ^{15}N-R_2, and $\{^1H\}$–^{15}N NOE data (Kay et al. 1989) using five models of increasing complexity (Mandel et al. 1995) that are derived from the original formulation of Lipari and Szabo (model 2) (Lipari and Szabo 1982) as extended by Clore (Clore et al. 1990) to two separated timescales of internal motion, fast (τ_f) and slow (τ_s) (or alternatively, first and second). In this approach, the spectral density is modeled as

$$J(\omega) = \frac{2}{5}\sum_{i=0}^{2} A_i\left[\frac{S^2\tau_i}{1+(\omega\tau_i)^2} + \frac{(1-S_f^2)\tau'_{f,i}}{1+(\omega\tau'_{f,i})^2} + \frac{(S_f^2-S^2)\tau'_{s,i}}{1+(\omega\tau'_{s,i})^2}\right] \quad (1)$$

where the square of the overall order parameter is the product of the order parameters for the first and second internal motions, $S^2 = S_f^2 S_s^2$, and the effective correlation times are given below. All five forms of the spectral density take into account the axially symmetric anisotropic rotational diffusion tensor by using the following external correlation function:

$$C_0^{axial}(t) = \frac{1}{5}(A_0 e^{-t/\tau_0} + A_1 e^{-t/\tau_1} + A_2 e^{-t/\tau_2}) \quad (2)$$

where, $A_0 = (1.5cos^2\alpha - 0.5)^2$, $A_1 = 3sin^2\alpha\, cos^2\alpha$, and $A_2 = 0.75sin^4\alpha$, with α being the angle between the N-H bond vector and the unique axis of the rotational diffusion tensor (Barbato et al. 1992). The five models, their parameters, and their spectral density functions are listed in Table 1, where, $\frac{1}{\tau'_i} = \frac{1}{\tau_i} + \frac{1}{\tau_e}$, $\tau_0 = (6D_\perp)^{-1}$, $\tau_1 = (D_\parallel + 5D_\perp)^{-1}$, and $\tau_2 = (4D_\parallel + 2D_\perp)^{-1}$.

Table 1 Model types, parameter subsets, and spectral density functions for MFA

Model	Parameter subset	Spectral density function
1	S^2	$J(\omega) = \frac{2}{5}\sum_{i=0}^{2} A_i\left[\frac{S^2\tau_i}{1+(\omega\tau_i)^2}\right]$
2	S^2, τ_e (ps-ns)	$J(\omega) = \frac{2}{5}\sum_{i=0}^{2} A_i\left[\frac{S^2\tau_i}{1+(\omega\tau_i)^2} + \frac{(1-S^2)\tau'_i}{1+(\omega\tau'_i)^2}\right]$
3	S^2, R_{ex}	$J(\omega) = \frac{2}{5}\sum_{i=0}^{2} A_i\left[\frac{S^2\tau_i}{1+(\omega\tau_i)^2}\right]$, $R'_2 = R_2 + R_{ex}$
4	S^2, τ_e(ps-ns), R_{ex}	$J(\omega) = \frac{2}{5}\sum_{i=0}^{2} A_i\left[\frac{S^2\tau_i}{1+(\omega\tau_i)^2} + \frac{(1-S^2)\tau'_i}{1+(\omega\tau'_i)^2}\right]$, $R'_2 = R_2 + R_{ex}$
5	S_f^2, $S^2 = S_f^2 S_s^2$, τ_e(ns)	$J(\omega) = \frac{2}{5}\sum_{i=0}^{2} A_i\left[\frac{S^2\tau_i}{1+(\omega\tau_i)^2} + \frac{(S_f^2-S^2)\tau'_i}{1+(\omega\tau'_i)^2}\right]$

Models 1-4 assume a single timescale for the internal motions (S_s^2=1), and S^2 corresponds to internal motions happening on the pico- to nanosecond timescale. Models 1 and 3 also assume that the correlation time for the internal motions approaches 0 and applies to very fast timescale motions (τ_f < 20 ps). Models 2 and 4 include motions on the finite pico- to nanosecond timescale, $\tau_f = \tau_e$(ps-ns) (Mandel et al. 1995). Models 3 and 4 are derived from models 1

and 2, respectively, but include a non-zero exchange contribution, R_{ex}, that accounts for residual contributions from conformational exchange and pseudo-first-order processes occurring on the micro- to millisecond timescale and measured here at a CPMG frequency of 500 Hz (Bloom et al. 1965). Model 5 assumes two timescale internal motion: fast motions with a correlation time $\tau_f \rightarrow 0$ and order parameter S_f^2, and nanosecond timescale motion with correlation time $\tau_s = \tau_e$(ns) and order parameter S_s^2 (Clore et al. 1990).

Model selection was performed using the Akaike's Information Criteria (AIC), χ^2+2k, where $\chi^2 = \sum_{i=1}^{n}\left[(R_i - R'_i)^2/\sigma_i^2\right]$ measures the goodness of fit between the experimental (R) and back-calculated (R') relaxation data (Abragam 1961). Here, σ is the experimental error, i is the residue number, k is the number of adjustable parameters, and n is the size of the data set at each residue. The AIC has been shown to strike the correct balance between underfitting (selecting the simplest model) and overfitting (selecting an overly complex model) and has been shown to perform better in model selection than the use of critical values of the F-statistic (d'Auvergne and Gooley 2003). With only 3 experimentally derived relaxation parameters at a single field ($n=3$), models 4 and 5 have no degrees of freedom ($n=k=3$), and to further prevent overfitting the AIC for models 1-3 were first compared, and only if the lowest AIC was outside of the respective 99% confidence limits (AIC > 11.2 for k = 1; AIC > 10.5 for k = 2), were models 4 and 5 considered. Note that the probability density function for the AIC follows that of the chi-square distribution for n-k degrees of freedom but is displaced by 2k. This model selection approach follows the general outline of Mandel et al (Mandel et al. 1995) but with the AIC replacing the use of critical values of the F-statistic. As only measurements at a single field are reported, these results should be considered preliminary (**ref**). After model selection, errors for the various parameters were obtained via 500 Monte Carlo (MC) simulations.

CSP Titrations and Estimation of K_d

Chemical shift perturbations were used to estimate K_d by recording a series of ^{1}H-^{15}N HSQC experiments with varying concentrations of the inhibitor avibactam and a total protein concentration of 850 μM. After the initial protein-only experiments, avibactam was titrated to a final concentration of 10%, 20%, 80%, 120%, 150%, and 200% of the total protein concentration. The sample was equilibrated at 298 K for 5 minutes after each inhibitor addition. All data were processed and analyzed using the Mestrelab NMR software package (Mestrelab Research) and NMRLineGuru GUI (Feng et al. 2019; Pemberton et al. 2020).

Molecular Dynamics Simulations

The starting model for MD simulations was taken from the substrate-free Toho-1 β-lactamase R274N/R276N double mutant X-ray crystal structure (PDB ID: 2ZQ8) (Shimamura et al. 2009), with the sulfate ion found in the active site removed. All-atom MD simulations were performed on conformation A of the protein solvated with explicit water (TIP3P model) in a rectangular periodic water box using the CHARMM 36 force field (Huang and Mackerell 2013) within NAMD 2.13 (Phillips et al. 2005). Sodium counter ions were added to neutralize the net charge of the system. 1000-step energy minimization of just the protein using harmonic restraints with a spring constant of 500 kcal/(mol·Å^2) was first performed, followed by a second 1000-step energy minimization using similar restraints on the water molecules. The system was then gradually heated in a 100-ps MD simulation from an initial temperature of 0.5 K to a final temperature of 298 K. The lengths of bonds involving H atoms were fixed by the SHAKE algorithm (Ryckaert et al. 1977). The NPT ensemble and periodic boundary conditions were applied. A temperature of 298 K was maintained using a Langevin thermostat with a damping constant of 2 ps^{-1}, and the hybrid Nose-Hoover Langevin piston method was used to keep the pressure at 1 atm. The non-bonded interactions were truncated at 14 Å with a switching beginning at 12 Å. Long-range electrostatic interactions beyond the cutoff limit were treated by the particle mesh Ewald method. VMD (Humphrey et al. 1996) was used for visualization and graphical representation. After the simulation was equilibrated for 5 ns, 10 starting structures from well-distributed points in the trajectory between 2 and 5 ns were chosen. 14 ns trajectories were used to generate sets of structural ensembles under the same temperature and pressure. This window size was determined based on the approximate rotational correlation time for Toho-1 β-lactamase, estimated to be 14 ns at 298 K based on the ^{15}N-T_1/T_2 ratio (Gu et al. 2014; Pastor and Amero 2015).

In total, 28,000 structures were collected for each of the starting conformations and used to determine the backbone amide NH bond vector S^2 value for each residue (except proline) (Best et al. 2005). Explicit separation of the internal motions from the overall tumbling of the molecule was first achieved by aligning C$^\alpha$ backbone atoms of each MD

snapshot relative to a reference structure (the first structure of the trajectory). The normalized backbone amide bond vector of each residue was then expressed in Cartesian coordinates ($\hat{\mu}$ = [x(t), y(t), z(t)]), and the ensemble/time average derived S^2-value was calculated from the MD trajectory as (Best et al. 2005):

$$S^2 = \frac{3}{2}tr\left(\langle\Phi\rangle^2\right) - \frac{1}{2} = \frac{3}{2}\left(\langle x^2\rangle^2 + \langle y^2\rangle^2 + \langle z^2\rangle^2 + 2\langle xy\rangle^2 + 2\langle xz\rangle^2 + 2\langle yz\rangle^2\right) - \frac{1}{2} \quad (3)$$

where the 3 x 3 tensor $\Phi = \hat{\mu} \otimes \hat{\mu}$.

Sequence numbering

The sequence for Toho-1 β-lactamase starts at residue 25 and ends, after 263 residues and three gaps (positions 58, 239, and 253), at residue 290 (Ambler and Coulson 1991).

Results and Discussions

Backbone Chemical Shift Assignments

TROSY-based, triple resonance solution-state NMR experiments (Riek et al. 2000; Fernández and Wider 2003) were used to assign 245 of the 250 non-proline backbone resonances for U-^{2}H,^{13}C,^{15}N labeled samples of the Toho-1 β-lactamase. Triple resonance TROSY-HNCO and TROSY-HN(CO)CACB experiments were used to provide sequential correlations, while TROSY-HN(CA)CO and TROSY-HNCACB were used to provide intra-residue correlations and confirm sequential assignments.

The protein's modest α-helix content (approximately 40%) resulted in relatively well-dispersed ^{15}N-^{1}H correlations in the HSQC spectrum. Regions between 8.0 and 8.8 ppm in the ^{1}H dimension and 115 and 120 ppm in the ^{15}N dimension were still somewhat congested, so to partially combat this the indirect acquisition nitrogen dimensions in the HSQC based experiments were run to 60.12 ms (digital resolution 16.63 Hz). The ten proline residues, which introduced breaks in the residues' sequential linking, presented a second challenge to the assignments. Still, approximately 200 of the backbone resonances could be pre-assigned using synchronous inspection and strip comparisons of ^{15}N-^{1}H planes in CCPNMR (Skinner et al. 2016). These were used in concert with automated peak picking and probabilistic assignment using APES (Shin et al. 2006) and the I-PINE webserver (Bahrami et al. 2009; Lee et al. 2019) to assign 245 of the 250 non-proline backbone resonances − 237 with >99% confidence − as shown in Figs. 3 and 4.

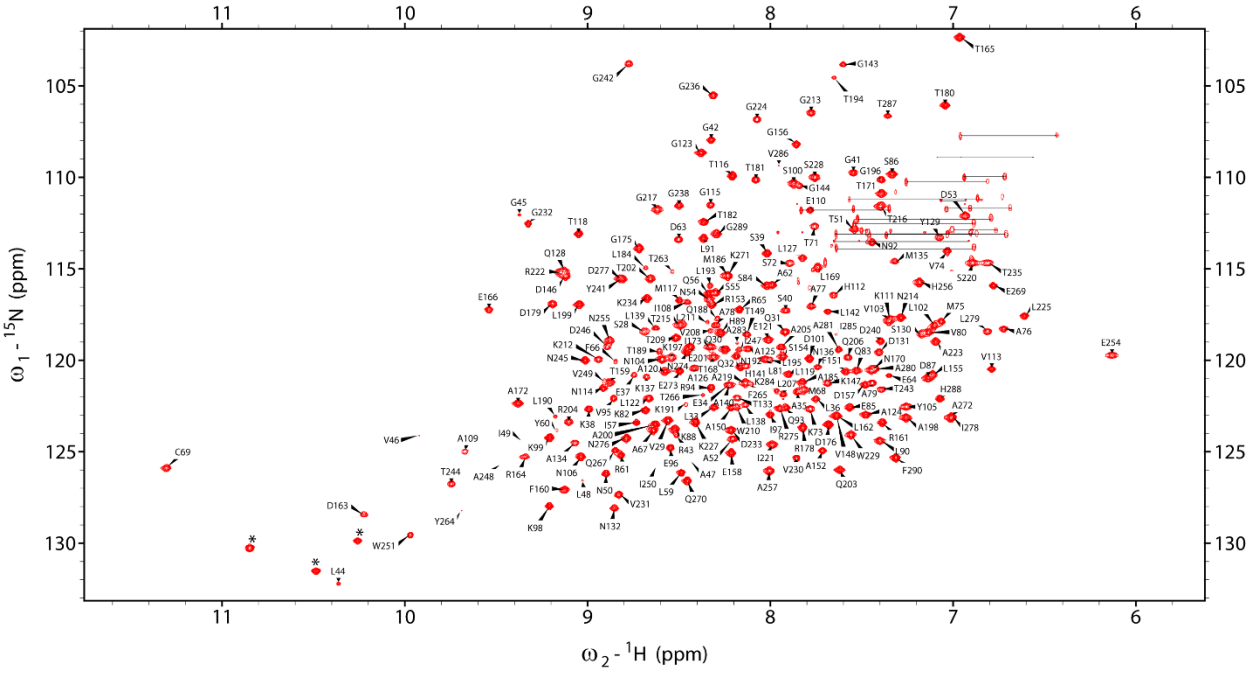

Fig. 3 Two-dimensional ^{15}N HSQC spectrum of U-^{2}H-^{13}C-^{15}N Toho-1 β-lactamase at 700 MHz (^{1}H), 298K, pH 6.5, and a protein concentration of 850 μM. The 237 labels indicate backbone amide ^{1}H and ^{15}N resonances that could be assigned with probability > 99%. Peaks connected by thin lines (upper right) correspond to correlations from the asparagine and glutamine side chain -NH_2 groups; peaks marked with an asterisk (bottom and bottom left) correspond to the sidechain correlations of arginine (folded) and to H^{ε}-N^{ε} correlations of tryptophan.

N-H correlations for the conserved active site residues S70 and S237 were not observed in the ^{15}N HSQC spectrum of the ligand-free enzyme. This was also true in the related Class-A β-lactamases PSE-4 and TEM-1 (Morin and Gagné 2009). Signal broadening due to either conformational dynamics inherent to the enzyme's active site or the absence of stabilizing interactions with a substrate could be responsible for the missing resonances. A complete absence of assignments was also observed for residues 258 to 262, presumably due to insufficient ^{1}H back exchange as these residues have modeled accessibility measures of zero (Esque et al. 2011) (see Fig S1, ESM).

In the presence of avibactam, the HSQC peak intensities for the active site residues K73 and D131 reduced to zero with increasing concentration of avibactam; at a 20% excess of avibactam, resonances for these residues were not observed. We ascribe this intensity loss to exchange broadening in the active site, which is supported by both neutron and X-ray crystal structures that show dual conformations of several key active site residues when a substrate is bound, including K73 and Y105 (Langan et al. 2018). Residues K73 and Y105 form several close contacts with residues Y129, S130, and N132, which dictate conformational changes of the amide group of D131. At the same time, strong signals for the ^{15}N-^{1}H correlations for residue S70 and S237 appeared in the spectrum for the bound protein with the amide proton (H^{N}) shift of S70 significantly downfield (10.12 ppm). Avibactam covalently linked to the side chain of S70 via a carbamoyl linkage presumably stabilizes this residue and eliminates exchange broadening, while the downfield shift is attributed to hydrogen bonding between the backbone amide and the strongly electronegative carbamoyl group. In the X-ray structure of avibactam bound to CTX-M-15 (PDB code: 4HBU), a closely related class A member, residue S237 forms a hydrogen bond to the carboxamide of avibactam and interacts with the sulfate group (Lahiri et al. 2013).

The backbone chemical shifts of ^{1}H, ^{15}N, and ^{13}C have been deposited at the Biological Magnetic Resonance Bank (BMRB) database (http://www.bmrb.wisc.edu) under accession number 50546. The backbone chemical shifts and their assignment probabilities are tabulated in Table S2 (ESM)

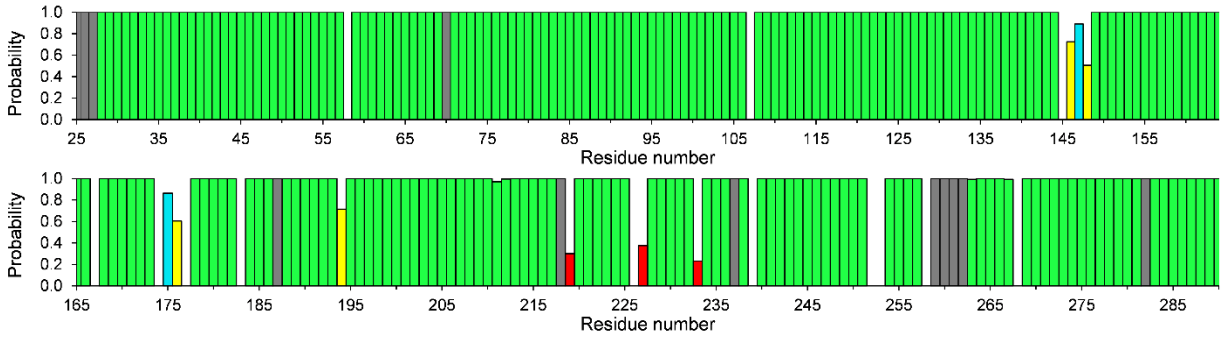

Fig. 4 Assignment probabilities for each residue of the ligand-free Toho-1 β-lactamase obtained using APES (Shin et al. 2006) and the I-PINE webserver (Bahrami et al. 2009; Lee et al. 2019). Color codes: green bars (> 99%); cyan bars (85% - 99%); yellow bars (50% - 85%); red bars (< 50%); gray bars (no assignment)

Prediction of Secondary Structure

Protein secondary structure was predicted based on the combination of the H^{N}, Cα, Cβ, CO, and N chemical shifts and the protein residue sequence using TALOS-N (Shen and Bax 2013), an artificial neural network-based hybrid system. Secondary structure predictions are summarized in Fig. 5, along with the difference between the C^{α} and C^{β} secondary chemical shifts. These can be compared to the secondary structure obtained from the X-ray crystal structure (PDB ID: 2ZQ8), also indicated in Fig. 5 and Table S2 (ESM). The secondary structure predictions from TALOS-N agree well with the secondary structure information obtained from X-ray diffraction. For the H6-Ω loop region (V155–D163),

and the N-terminal portion of the Ω loop (164–167), the secondary structure prediction points towards β-strand, while the X-ray crystal structure indicates a loop like region. The same is observed for the latter section of helix H11. The influence of the complex dynamics of these regions on the chemical shift could potentially be responsible for these discrepancies.

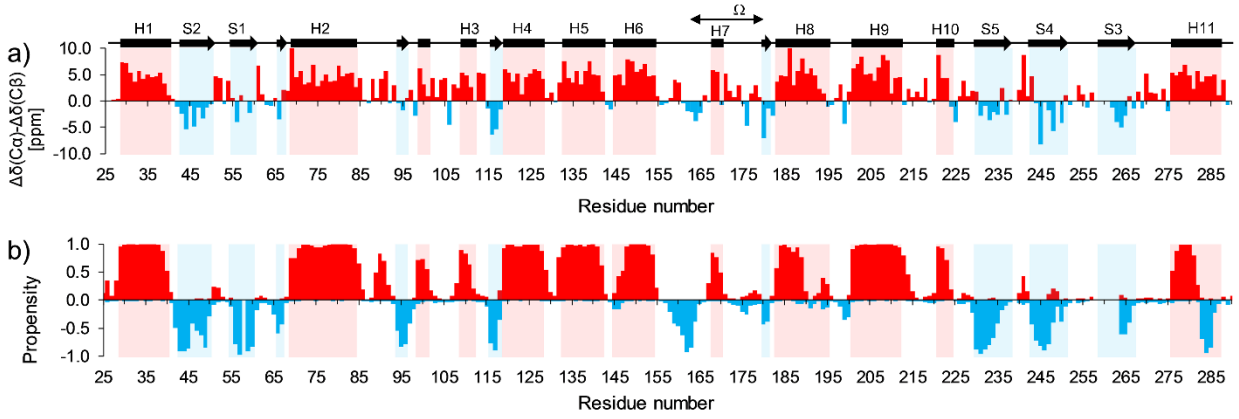

Fig. 5 (a) Difference between the C^{α} and C^{β} secondary chemical shifts (Mielke and Krishnan 2009) for Toho-1 β-lactamase. (b) Secondary structure predictions for Toho-1 β-lactamase from TALOS-N. The propensity of occurrence for α-helix is shown in red, and that for β-sheet is shown in blue and inverted. The presence of loops is indicated by the simultaneous presence of helix and strand probabilities. The secondary structure elements from the X-ray crystal structure are indicated across the top (bars α-helices, arrows β-strands) and by the faint red (α-helix) and blue (β-strand) color shades

Chemical Shift Perturbations and the Ligand Binding Site

The addition of avibactam led to chemical shift perturbations (CSPs) (Williamson 2013) in the ^{15}N HSQC spectrum of Toho-1 β-lactamase, as shown in Fig. S2 (ESM). The CSPs were quantified as the average chemical shift perturbation $\Delta\delta_{NH}$ (in ppm) based on the weighted root-mean-square of the proton and nitrogen chemical shift perturbations ($\Delta\delta_H$ and $\Delta\delta_N$, respectively), according to

$$\Delta\delta_{NH} = \sqrt{\frac{\Delta\delta_H^2 + 0.14\Delta\delta_N^2}{2}} \quad (4)$$

where the factor of 0.14 accounts for differences in sensitivity of the amide proton and nitrogen backbone resonances (Schumann et al. 2007). These are summarized in Fig. 6.

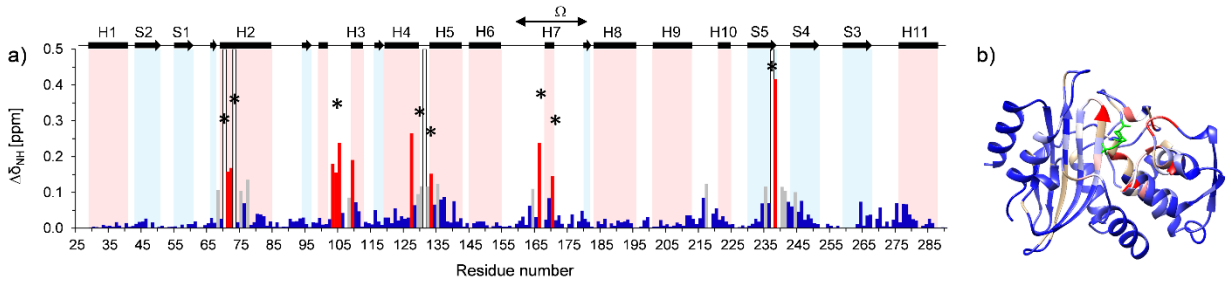

Fig. 6 (a) Average chemical shift perturbations ($\Delta\delta_{NH}$) calculated for residues of Toho-1 β-lactamase at a protein concentration of 850 μM and a [inhibitor]/[protein] ratio of 1.2. Red indicates residues that show relatively large CSPs, gray indicates residues with moderate CSPs, while blue indicates residues with low CSPs; hollow bars represent residues whose correlations either become indiscernible or appear upon the addition of avibactam at the final concentration of 1.2 times that of the protein. Asterisks are placed over active-site residues S70, K73, N104, S130, N132, E166, N170, and S237 that participate in catalysis and display relatively large CSPs themselves or in their sequential neighborhood. The secondary structure elements from the X-ray crystal structure are indicated across the top (bars α-helices, arrows β-strands). (b) Mapping of the avibactam binding site onto the Toho-1 β-lactamase crystal structure 2ZQ8 from CSPs. The coordinates of avibactam were extracted from crystal structure 4HBU after alignment with 2ZQ8

The most significant CSPs were found for residues S70, K73, N104, S130, N132, E166, N170, and S237, marked with asterisks in Fig. 6a. The relatively large CSPs observed for these residues allowed for the mapping of the ligand-binding site (Fig. 6b). The CSPs can be rationalized from ligand atom interactions with catalytic residues, as observed in the X-ray crystal structure of the related protein CTX-M-15 complexed with avibactam (PDB ID: 4HBU) and 100 ns MD simulation of the CTX-M-15 covalent complex (Lahiri et al. 2013; Lizana and Delgado 2019). Analysis of the MD trajectory showed that residues C69, N104, N132, E166, and N170 make contact with the carbonyl oxygen of the acylamide side chain of avibactam and that residues K234, S237, T235, and R274 make polar contacts to the negatively charged sulfate group. The side chain of S130 hydrogen bonds with the amine linkage to the sulfate group, and the piperidine ring forms a hydrophobic stack with the Y105 side chain. The range of CSPs observed for the binding of avibactam to Toho-1 β-lactamase was small, possibly because the sulfate group of avibactam can adopt a range of bound conformations, as observed in the MD trajectory, and therefore the perturbations in chemical shifts are averaged.

Ligand-titration experiments, in which the ^{15}N-HSQC chemical shift perturbations were followed as a function of the total added inhibitor, were also performed to quantify the dissociation constant (K_d) as described in the ESM. The majority of the CSPs showed a characteristic very tight binding titration curve. These binding curves signified slow exchange, 1:1 binding, and allowed only an upper limit of the binding constant to be estimated, $K_d < 1.0$ μM (Fielding 2007; Williamson 2013). These results are consistent with an essentially irreversible (on the NMR timescale) covalent bond being formed between inhibitor and protein. Isothermal titration calorimetry measurements for the related TEM-1with avibactam reported K_d, to be in the lower nanomolar range (Ehmann et al. 2012).

Backbone Dynamics from Model-Free Analysis of Relaxation Experiments and MD Simulations

The high quality of the NMR spectra allowed the measurement of site-specific ^{15}N-R_1, R_2, and {^{1}H}-^{15}N NOE for 236 of the 263 residues before and after the addition of avibactam; these initial experiments were performed at a single field of 16.44 T. The data are summarized in Fig. 7 and provide a window into the backbone dynamics of the protein scaffold (Kay 1998). As is typical, the loop regions and the N- and C-termini were found to be more dynamic on the pico- to nanosecond timescale than the rest of the protein, displaying increased ^{15}N-R_1 relaxation rates and decreased ^{15}N-R_2 relaxation rates. At the same time, increased dynamics on the micro- to millisecond timescale could be identified for residues in β-strands S1, S2, and S3, and α-helices H4, H8, and H11 based on increased ^{15}N-R_2 relaxation rates as highlighted in the plot of the ^{15}N-R_2/R_1 ratio (Fig. 7d). Residues exhibiting large deviations in the ^{15}N-R_2/R_1 plot due to anisotropic motion could be separated from those undergoing residual exchange broadening by plotting the product of the relaxation rates, $R_2 \times R_1$, (Fig. 7e) as motional anisotropy affects ^{15}N-R_1 and ^{15}N-R_2 in opposite ways

(Kneller et al. 2002). Effective R_{ex} terms were estimated by the method of Bracken for residues displayed in Fig. 8c for which the product of their relaxation rates deviated significantly from the average (Kneller et al. 2002; Spyracopoulos 2006).

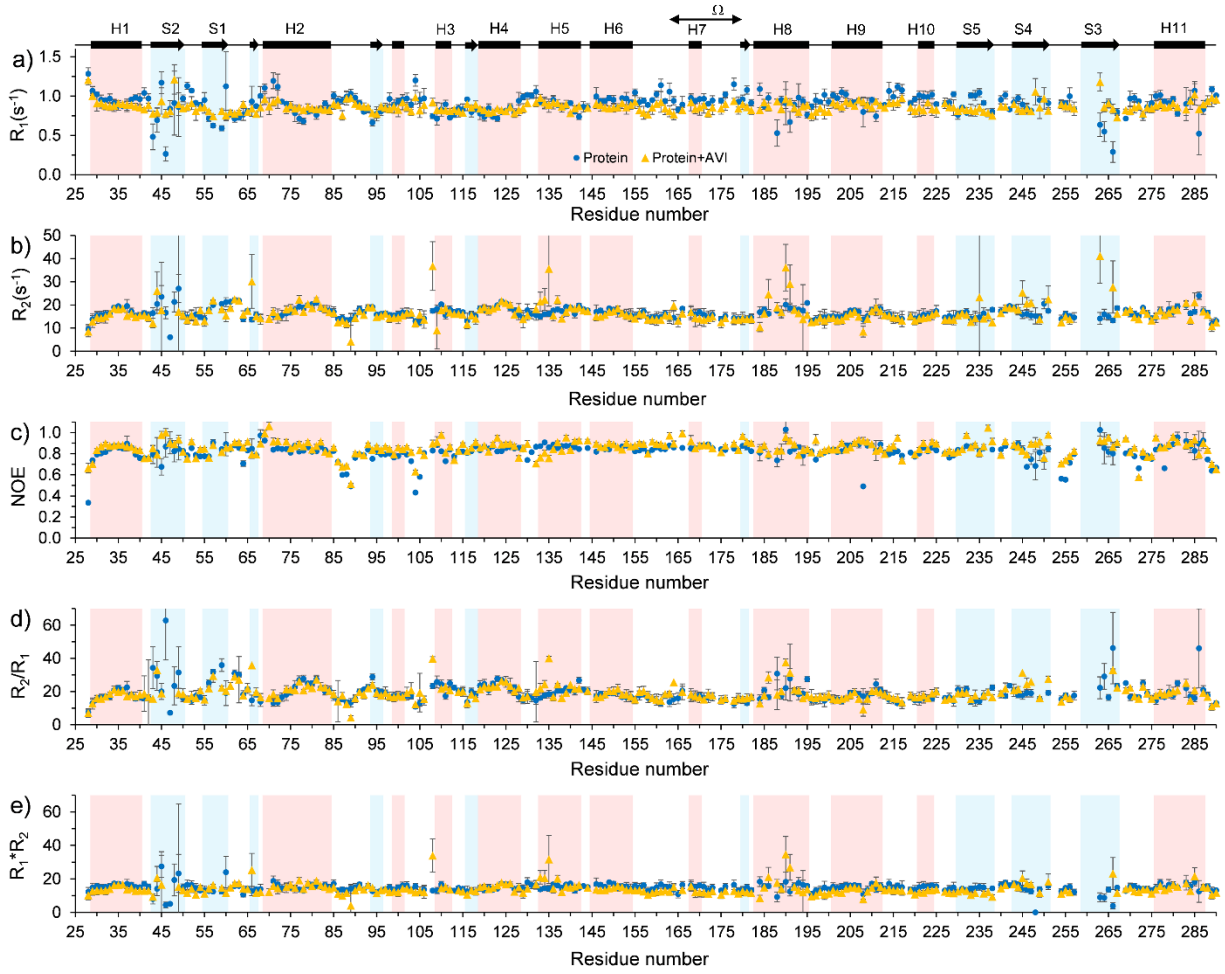

Fig. 7 Experimental (a) ^{15}N-R_1 and (b) ^{15}N-R_2 relaxation times and (c)$\{^1$H$\}$-^{15}N NOE for residues of Toho-1 β-lactamase with (orange triangles) and without (blue circles) avibactam at 700 MHz, 298K, a protein concentration of 850 μM, and [inhibitor]/[protein] ratio of 1.2. (d) The ratio of residue-wise relaxation rates ^{15}N-R_2/R_1, and (e) their products ^{15}N-$R_2 \times R_1$

To characterize the dynamics quantitively, model-free analysis was implemented (Spyracopoulos 2006) using five models of increasing complexity (Table 1). The Akaike's Information Criteria (AIC) was used to select the best-fit model of residue-specific internal motional parameters (d'Auvergne and Gooley 2003). The five models are described in the *Experimental* section and summarized in Table 1. For the ligand-free protein, 61 residues were fit to model 1 and 21 residues were fit to model 3; for these residues the internal motions were fast enough that their net effect on relaxation was observed only as a reduction in the order parameter from 1 to S^2, plus a potential exchange contribution. 102 residues were fit to model 2, and 8 to model 4; for these residues, single time-scale internal motions on the pico- to nanosecond timescale contributed significantly to the observed relaxation. 27 residue was fit to model 5, indicating that internal motions on two timescales contributed to their relaxation. Finally, 15 residues were not fit well by any model (AIC>20), presumably demanding a more complex spectral density function to represent their dynamics.

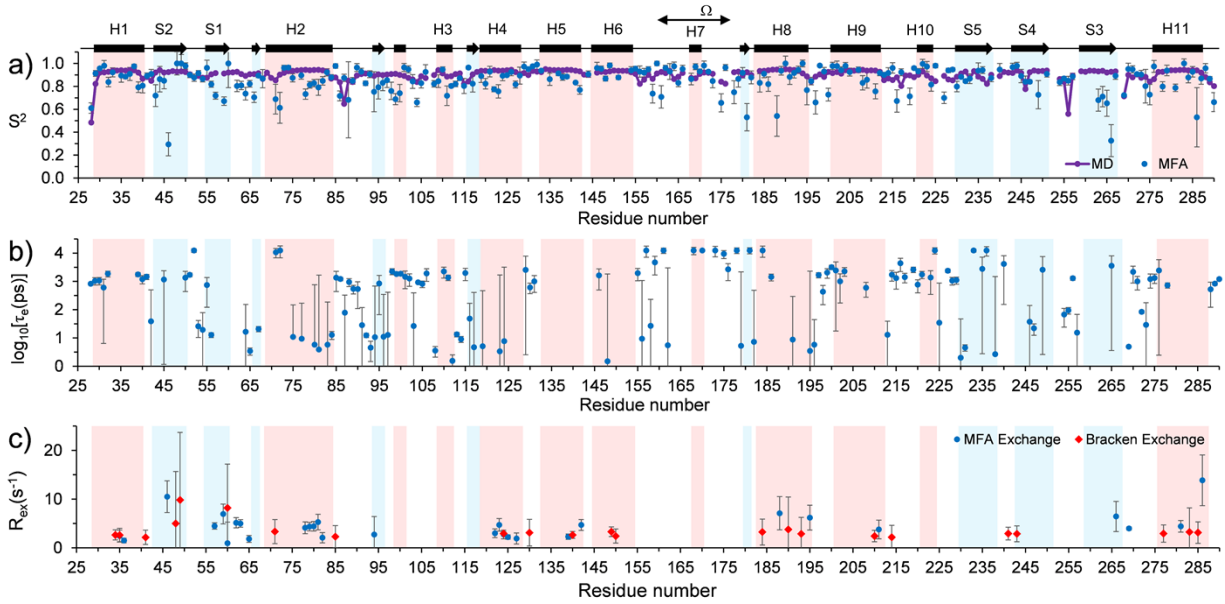

Fig. 8 Dynamical parameters for the Toho-1 β-lactamase. (a) Residue-wise MD (purple circles) and MFA (blue circles) derived order parameters, S^2 (b) Local correlation times on the pico-to nanosecond scale from MFA (c) Conformational exchange contributions, R_{ex}, for ligand-free Toho-1 β-lactamase derived from MFA (blue circles) and the method of Bracken (red diamonds). Analysis for data acquired at 700 MHz (^{1}H), 298K, and protein concentration of 850 μM.

As summarized in Fig. 8, the results of MFA indicate that Toho-1 β-lactamase is a well-ordered protein, with an average generalized order parameter of 0.86. This high order includes the active site, with many residues displaying $S^2 > 0.85$, and residues that interact with substrate, K73, S130, S132, E166, N170, and T235, having order parameters of 0.96, 0.95, 0.99, 0.95, 0.93, and 0.94, respectively. 29 residues have an explicit exchange parameter, R_{ex}, highlighting the presence of micro- to millisecond motions. The H6-Ω loop region and the entire Ω loop were found to be as rigid on the pico- to nanosecond timescale as the rest of the protein, with an average S^2 value of 0.89.

MFA was also applied to the Toho-1 β-lactamase in complex with the inhibitor avibactam. For the inhibitor-bound enzyme, 99 residues were fit to model 1, 53 were fit to model 2, 14 residues were fit to model 3, 3 to model 4, and 13 to model 5. 49 residues were not fit well by any model, which may be indicative of more complex dynamics for the inhibitor-enzyme adduct. The residue-specific dynamical parameters are summarized in Fig. 9. Upon binding of avibactam, the inhibitor-enzyme complex remains well-ordered, with an average generalized order parameter of 0.85, while the dynamics move to a faster timescale (shorter correlation time), with fewer residues chosen for models 2, 4, and 5. Notably, there is a slight decrease in the order parameters for the active site residues interacting with the inhibitor, with residues S130, S132, N170, and T235 showing reduced order parameters of 0.92, 0.92, 0.84, and 0.89, respectively, while E166 is no longer fit well by any model (S^2 = 0.85, but AIC=34.62). There is also a modest decrease in order parameters for residues in the Ω loop region, with a new average value of 0.83. While there are additional, subtle changes in the dynamical parameters upon binding of avibactam that can be identified in Fig. 9, a more comprehensive analysis of the fast pico- to nanosecond timescale dynamics will require relaxation data at multiple fields.

For the active site residues, the increase in the amplitude of dynamics on the pico- to nanosecond timescale is accompanied by a concomitant increase in dynamics on the slower micro- to millisecond times suggested by the loss of the HSQC peak intensities for the active site residues K73 and D131. This was further examined by initial CPMG relaxation dispersion (CPMG RD) experiments performed again at a single field of 16.4 T (700 MHz ^{1}H). The CPMG-RD exchange rate, R_{ex}(CPMG-RD), was calculated as the difference in apparent transverse relaxation rate (R_2') measured at effective fields of υ_{CPMG} = 25 Hz and 1000 Hz. Significant refocusing of magnetization under CPMG occurs when the CPMG rate is greater than twice the rate of the dynamics (Kleckner and Foster 2011), making

R_{ex}(CPMG-RD) as defined here most sensitive to millisecond timescale motions. As seen in Fig. 10, there is a stark increase in millisecond timescale dynamics within the active site upon binding of avibactam. Millisecond timescale motions are expected to play an important role in catalytic promiscuity, as discussed below.

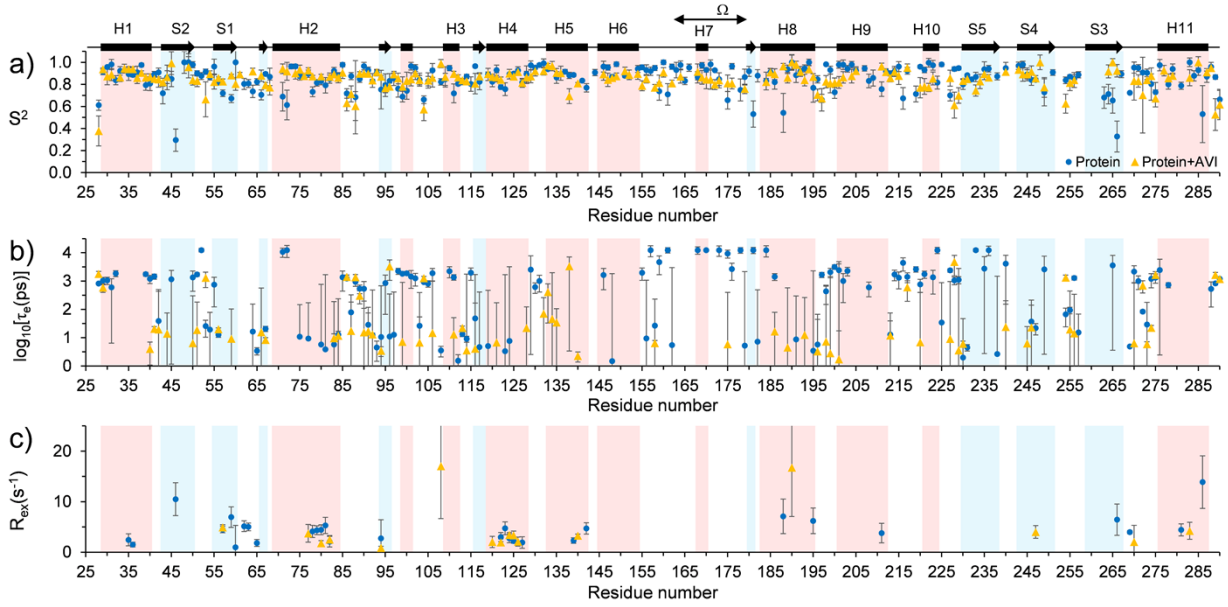

Fig. 9 Residue-wise MFA derived (a) S^2, (b) local correlation times on the pico-to nanosecond scale, and (c) conformational exchange contributions for Toho-1 β-lactamase with (orange triangles) and without (blue circles) avibactam at 700 MHz (^{1}H), 298K, a protein concentration of 850 μM, and [inhibitor]/[protein] = 1.2.

MD simulations of inhibitor-free Toho-1 β-lactamase were also performed and found to accurately reproduce the MFA order parameters for regions of the protein with well-defined secondary structures (Fig. 8). The largest discrepancies between simulated and experimental S^2 values were found in secondary structures S1, H2, and H5, for which residual exchange contributions on the milli- to microsecond timescale were identified in the MFA. This disagreement can potentially be attributed to differences in empirical and experimental time scales and insufficient conformational sampling during the 14 ns window of the MD simulations. Small discrepancies were also observed within the Ω loop, although the deviations between simulated and experimental order parameters for the Toho-1 β-lactamase are substantially smaller than those previously reported for the Ω loop in other class A members TEM-1 and PSE-4 (Fisette et al. 2010; Fisette et al. 2012).

Three additional class-A β lactamases have been characterized with MFA: TEM-1, PSE-4, and BlaC (Savard and Gagné 2006; Morin and Gagné 2009; Fisette et al. 2010; Elings et al. 2020). This class of enzymes shows similar dynamic features, including being well-ordered overall and having active sites that are mostly rigid on the pico- to nanosecond timescale, while displaying microsecond-to-millisecond motions for key catalytic residues such as S70 and S237 (or their flanking residues). It was originally proposed for TEM-1 that the high degree of order for the apo form could indicate that catalytic residues are appropriately positioned to play their role as soon as the substrate enters the active site (Savard and Gagné 2006). Such a high degree of ordering may also help mitigate any potentially unfavorable changes in conformational entropy upon substrate binding. Both the Toho-1 β-lactamase and BlaC have been characterized in complex with the inhibitor avibactam. Notably the active sites of both display larger amplitude dynamics on the microsecond-millisecond timescales upon inhibitor binding. These induced active site dynamics are thought to assist catalytic promiscuity by accommodating variously sized substrates and increasing the probability of sampling the optimal conformation for hydrolysis of the bound ligand (Elings et al. 2020). These slower motions may also be relevant for catalysis by facilitating substrate entry and product release.

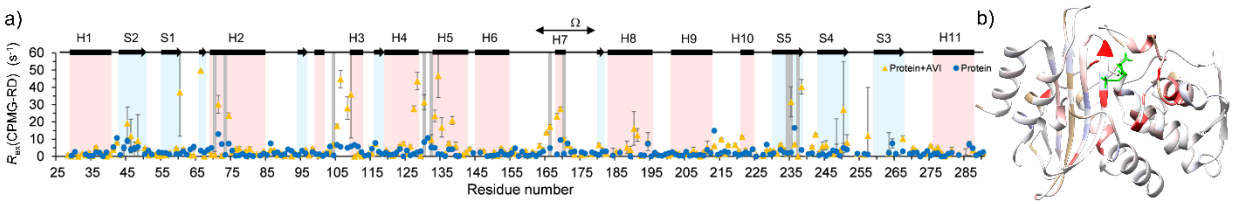

Fig. 10. (a) CPMG relaxation dispersion exchange rates for residues of the Toho-1 β-lactamase with (orange triangles) and without (blue circles) avibactam at 700 MHz (^{1}H) and 298K from. The CPMG-RD exchange rate is calculated as the difference between R_2' at υ_{CPMG} = 25 s^{-1} and R_2' at υ_{CPMG} = 1,000 s^{-1} and reports primarily on millisecond timescale motions. Grey bars indicate active site residues that interact with avibactam. (b) Changes in CPMG exchange rates upon binding of avibactam mapped onto the Toho-1 β-lactamase crystal structure 2ZQ8. Red indicates residues that become more dynamic upon inhibitor addition, blue indicates residues that rigidify, and white indicates no change

Conclusion

Sequential assignments of backbone C, N, and H^N chemical shifts for the Toho-1 β-lactamase R274N/R276N double mutant were accomplished using 2D and 3D TROSY-based NMR experiments. These assignments permitted the prediction of secondary structure that compares well to the structure obtained from X-ray diffraction. The chemical shift assignments also enabled the site-specific characterization of inhibitor binding. Titration with the non β-lactam β-lactamase inhibitor avibactam was found to give perturbations in backbone chemical shifts indicative of slow exchange, 1:1 tight binding that are consistent with essentially irreversible covalent binding of the inhibitor on the NMR timescale. The extended lifetime of the inhibitor-enzyme complex allowed site-specific relaxation rates to be measured. Model-free analysis of the ^{15}N relaxation data revealed well-ordered structures for the ligand-free and avibactam-bound forms with generalized order parameters of 0.86 and 0.85, respectively. The high degree of ordering on the pico- to nanosecond timescale for the free enzyme is thought to allow precise positioning of the sidechains for catalysis and help mitigate any potentially unfavorable changes in conformational entropy upon substrate binding. Complementary relaxation dispersion experiments show that upon substrate binding, there is actually a significant upturn in active site motions on the millisecond timescale. Promiscuous enzymes are expected to exhibit active-site flexibility to help accommodate variously sized substrates and increase the probability of sampling the optimal conformation for catalysis. The combination of high rigidity on short timescales and active site flexibility on longer timescales is consistent with the hypotheses of dynamical duality: the Toho-1 β-lactamase is rigid on the pico- to nanosecond timescale but exhibits flexibility on the millisecond timescale in and around the active site, as observed for other members of the class-A β-lactamases.

The assignment of backbone chemical shifts and the characterization of dynamics of the Toho-1 β-lactamase highlight a need for complementary data focusing on the protonation states of the catalytic residues' sidechains (Damblon et al. 1996; Pemberton et al. 2020). This motivates the ongoing investigation of the detailed chemical structure for Toho-1 β-lactamase using NMR and other techniques to better understand the catalytic cycle of the modern members of Class-A β-lactamases.

Data Availability

The backbone chemical shifts of ^{1}H, ^{15}N, and ^{13}C have been deposited at the Biological Magnetic Resonance Bank (BMRB) database (http://www.bmrb.wisc.edu) under accession number 50546. The backbone chemical shift and their assignment probabilities are tabulated in Table S2 (ESM). Additional data are freely available from the authors upon request.

Acknowledgments

The research reported in this publication was supported in part by NSF grant CHE1710671 (LJM) and NIH grant GM097569 (LJM). This research used resources at the Spallation Neutron Source and the High Flux Isotope Reactor, which are DOE Office of Science User Facilities operated by the Oak Ridge National Laboratory. The Office of Biological and Environmental Research supported research at ORNL's Center for Structural Molecular Biology (CSMB), a DOE Office of Science User Facility. This research used resources at the Second Target Station, which is a DOE Office of Science User Facilities Construction Project at Oak Ridge National Laboratory.

References

Abragam A (1961) The Principles of Nuclear Magnetism. Clarendon Press, Oxford

Ambler RP, Coulson AFW (1991) A standard numbering scheme for the Class A beta-lactamases. Biochem J 276:1990–1991

Bahrami A, Assadi AH, Markley JL, Eghbalnia HR (2009) Probabilistic Interaction Network of Evidence Algorithm and its Application to Complete Labeling of Peak Lists from Protein NMR Spectroscopy. PLoS Comput Biol 5:1–15 . https://doi.org/10.1371/journal.pcbi.1000307

Banerjee S, Pieper U, Kapadia G, Pannell LK, Herzbere O (1998) Role of the Ω-loop in the activity, substrate specificity, and structure of class A β-lactamase. Biochemistry 37:3286–3296 . https://doi.org/10.1021/bi972127f

Barbato G, Ikura M, Kay LE, Pastor RW, Bax A (1992) Backbone Dynamics of Calmodulin Studied by 15N Relaxation Using Inverse Detected Two-Dimensional NMR Spectrocopy: The Central Helix Is Flexible. Biochemistry 31:5269–5278

Bebrone C, Lassaux P, Vercheval L, Sohier JS, Jehaes A, Sauvage E, Galleni M (2010) Current challenges in antimicrobial chemotherapy: Focus on β-lactamase inhibition. Drugs 70:651–679 . https://doi.org/10.2165/11318430-000000000-00000

Best RB, Clarke J, Karplus M, Pasteur L (2005) What Contributions to Protein Side-chain Dynamics are Probed by NMR Experiments ? A Molecular Dynamics Simulation Analysis. J Mol Biol 349:185–203 . https://doi.org/10.1016/j.jmb.2005.03.001

Bloom M, Reeves LW, Wells EJ (1965) Spin Echoes and Chemical Exchange. J Chem Phys 42:1615–1624 . https://doi.org/10.1063/1.1696168

Bush K (2010) Bench-to-bedside review: The role of β-lactamases in antibiotic-resistant Gram-negative infections. Crit Care 14:224–232 . https://doi.org/10.1186/cc8892

Bush K (2013) The ABCD's of β-lactamase nomenclature. J Infect Chemother 19:549–559 . https://doi.org/10.1007/s10156-013-0640-7

Cavanagh J, Fairbrother W, Palmer III A, Rance M, Skelton N (2007) Protein NMR Spectroscopy: principles and practice, 2nd edn. Elsevier Inc., San Diego

Clore GM, Szabo A, Bax A, Kay LE, Driscoll PC, Gronenborn AM (1990) Deviations from the Simple Two-Parameter Model-Free Approach to the Interpretation of Nitrogen-15 Nuclear Magnetic Relaxation of Proteins. J Am Chem Soc 112:4989–4991 . https://doi.org/10.1021/ja00168a070

Cortina GA, Kasson PM (2016) Excess positional mutual information predicts both local and allosteric mutations affecting beta lactamase drug resistance. Bioinformatics 32:3420–3427 . https://doi.org/10.1093/bioinformatics/btw492

d'Auvergne EJ, Gooley PR (2003) The use of model selection in the model-free analysis of protein dynamics. J Biomol NMR 25:25–39 . https://doi.org/10.1023/A:1021902006114

Damblon C, Raquet X, Lian L, Lamotte-brasseur J, Fonze E, Charlier P, Roberts GCK, Frère J (1996) The Catalytic Mechanism of β -Lactamases : NMR Titration of an Active-Site Lysine Residue of the TEM-1 Enzyme. PNAS 93:1747–1752

Drawz SM, Bonomo RA (2010) Three decades of β-lactamase inhibitors. Clin Microbiol Rev 23:160–201 . https://doi.org/10.1128/CMR.00037-09

Ehmann DE, Jahić H, Ross PL, Gu RF, Hu J, Kern G, Walkup GK, Fisher SL (2012) Avibactam is a covalent, reversible, non-β-lactam β-lactamase inhibitor. Proc Natl Acad Sci U S A 109:11663–11668 . https://doi.org/10.1073/pnas.1205073109

Elings W, Gaur A, J. Blok A, Timmer M, van Ingen H, Ubbink M (2020) □-Lactamase of Mycobacterium tuberculosis Shows Dynamics in the Active Site That Increase upon Inhibitor Binding Wouter. Antimicrob Agents Chemother 64:1–13

Esque J, Oguey C, Brevern AG De, Pontoise DC, Chauvin A (2011) Comparative Analysis of Threshold and Tessellation Methods for Determining Protein Contacts. J Chem Inf Model 51:493–507 . https://doi.org/10.1021/ci100195t

Feng C, Kovrigin EL, Post CB (2019) NmrLineGuru: Standalone and User-Friendly GUIs for Fast 1D NMR Lineshape Simulation and Analysis of Multi-State Equilibrium Binding Models. Sci Rep 9:1–14 . https://doi.org/10.1038/s41598-019-52451-8

Fernández C, Wider G (2003) TROSY in NMR studies of the structure and function of large biological macromolecules. Curr Opin Struct Biol 13:570–580 . https://doi.org/10.1016/j.sbi.2003.09.009

Fielding L (2007) NMR methods for the determination of protein – ligand dissociation constants. Princ Nucl Magnaetic Reson Spectrosc 51:219–242 . https://doi.org/10.1016/j.pnmrs.2007.04.001

Fisette O, Gagné SM, Lagüe P (2012) Molecular dynamics of class A β-lactamases - Effects of substrate binding. Biophys J 103:1790–1801 . https://doi.org/10.1016/j.bpj.2012.09.009

Fisette O, Morin S, Savard PY, Lagüe P, Gagné SM (2010) TEM-1 backbone dynamics - Insights from combined molecular dynamics and nuclear magnetic resonance. Biophys J 98:637–645 . https://doi.org/10.1016/j.bpj.2009.08.061

Gu Y, Li D-W, Brüschweiler R (2014) NMR Order Parameter Determination from Long Molecular Dynamics Trajectories for Objective Comparison with Experiment. J Chem Theory Comput 10:2599–2607 . https://doi.org/10.1021/ct500181v

Hart KM, Ho CMW, Dutta S, Gross ML, Bowman GR (2016) Modelling proteins' hidden conformations to predict antibiotic resistance. Nat Commun 7:1–10 . https://doi.org/10.1038/ncomms12965

Helfand MS, Totir MA, Carey MP, Hujer AM, Bonomo RA, Carey PR (2003) Following the Reactions of Mechanism-Based Inhibitors with β-Lactamase by Raman Crystallography. Biochemistry 42:13386–13392 . https://doi.org/10.1021/bi035716w

Huang J, Mackerell AD (2013) CHARMM36 All-Atom Additive Protein Force Field: Validation Based on Comparison to NMR Data. J Comput Chem 34:2135–2145 . https://doi.org/10.1002/jcc.23354

Humphrey W, Dalke A, Schulten K (1996) VMD: Visual Molecular Dynamics. J Mol Graph 14:33–38 . https://doi.org/10.1016/0263-7855(96)00018-5

Ishii Y, Ohno A, Taguchi H, Imajo S, Ishiguro M, Matsuzawa H (1995) Cloning and Sequence of the Gene Encoding a Cefotaxime-Hydrolyzing Class A β-lactamase Isolated from Escherichia coli. Antimicrob Agents Chemother 39:2269–2275 . https://doi.org/10.1128/AAC.39.10.2269

Ishima R, Torchia DA (2005) Error estimation and global fitting in transverse-relaxation dispersion experiments to determine chemical-exchange parameters. J Biomol NMR 32:41–54 . https://doi.org/10.1007/s10858-005-3593-z

Jacoby GA (2006) MINIREVIEW Beta-Lactamase Nomenclature. Antimicrob Agents Chemother 50:1123–1129 . https://doi.org/10.1128/AAC.50.4.1123

Kay LE (1998) Protein dynamics from NMR. Biochem Cell Biol 76:145–152 . https://doi.org/10.1038/755

Kay LE, Torchia DA, Bax A (1989) Backbone Dynamics of Proteins As Studied by 15N Inverse Detected Heteronuclear NMR Spectroscopy: Application to Staphylococcal Nuclease. Biochemistry 28:8972–8979

King DT, King AM, Lal SM, Wright GD, Strynadka NCJ (2016) Molecular Mechanism of Avibactam-Mediated β-Lactamase Inhibition. ACS Infect Dis 1:175–184 . https://doi.org/10.1021/acsinfecdis.5b00007

Kleckner IR, Foster MP (2011) An introduction to NMR-based approaches for measuring protein dynamics. Biochim Biophys Acta - Proteins Proteomics 1814:942–968 . https://doi.org/10.1016/j.bbapap.2010.10.012

Kneller JM, Lu M, Bracken C (2002) An Effective Method for the Discrimination of Motional Anisotropy and Chemical Exchange. J Am Chem Soc 124:1852–1853 . https://doi.org/10.1021/ja017461k

Kong KF, Schneper L, Mathee K (2010) Beta-lactam antibiotics: From antibiosis to resistance and bacteriology. APMIS 118:1–36 . https://doi.org/10.1111/j.1600-0463.2009.02563.x

Lagacé-Wiens P, Walkty A, Karlowsky JA (2014) Ceftazidime-avibactam: An evidence-based review of its pharmacology and potential use in the treatment of Gram-negative bacterial infections. Core Evid 9:13–25 . https://doi.org/10.2147/CE.S40698

Lahiri SD, Mangani S, Durand-Reville T, Benvenuti M, De Luca F, Sanyal G, Docquierd J-D (2013) Structural Insight into Potent Broad-Spectrum Inhibition with Reversible Recyclization Mechanism : Avibactam in Complex with CTX-M-15 and Pseudomonas aeruginosa AmpC β-Lactamases. Antimicrob Agents Chemother 57:2496–2505 . https://doi.org/10.1128/AAC.02247-12

Langan PS, Sullivan B, Weiss KL, Coates L (2020) Probing the role of the conserved residue Glu166 in a class A β-lactamase using neutron and X-ray protein crystallography. Acta Crystallogr Sect D Struct Biol 76:118–123 . https://doi.org/10.1107/S2059798319016334

Langan PS, Vandavasi VG, Cooper SJ, Weiss KL, Ginell SL, Parks JM, Coates L (2018) Substrate Binding Induces Conformational Changes in a Class A β-lactamase That Prime It for Catalysis. ACS Catal 8:2428–2437 . https://doi.org/10.1021/acscatal.7b04114

Langan PS, Vandavasi VG, Weiss KL, Cooper JB, Ginell SL, Coates L (2016) The structure of Toho1 β-lactamase in complex with penicillin reveals the role of Tyr105 in substrate recognition. FEBS Open Bio 6:1170–1177 . https://doi.org/10.1002/2211-5463.12132

Lee W, Bahrami A, Dashti HT, Eghbalnia HR, Tonelli M, Westler WM, Markley JL (2019) I-PINE web server: an integrative probabilistic NMR assignment system for proteins. J Biomol NMR 73:213–222 . https://doi.org/10.1007/s10858-019-00255-3

Lee W, Markley JL (2018) PINE-SPARKY.2 for automated NMR-based protein structure research. Bioinformatics 34:1586–1588 . https://doi.org/10.1093/bioinformatics/btx785

Lee W, Tonelli M, Markley JL (2015) NMRFAM-SPARKY: enhanced software for biomolecular NMR spectroscopy. Bioinformatics 31:1325–1327 . https://doi.org/10.1093/bioinformatics/btu830

Lipari G, Szabo A (1982) Model-Free Approach to the Interpretation of Nuclear Magnetic Resonance Relaxation in Macromolecules. 1. Theory And Range Of Validity. J Am Chem Soc 104:4546–4559 . https://doi.org/10.1002/chin.198247060

Lizana I, Delgado EJ (2018) Theoretical insights on the inhibition mechanism of a class A Serine Hydrolase by avibactam. J Comput Chem 39:1943–1948 . https://doi.org/10.1002/jcc.25340

Lizana I, Delgado EJ (2019) Molecular Insights on the Release of Avibactam from the Acyl-Enzyme Complex. Biophys J 116:1650–1657 . https://doi.org/10.1016/j.bpj.2019.03.027

Lobkovsky E, Moews PC, Liu H, Zhao H, Frere JM, Knox JR (1993) Evolution of an enzyme activity: Crystallographic structure at 2-Å resolution of cephalosporinase from the ampC gene of Enterobacter cloacae P99 and comparison with a class a penicillinase. Proc Natl Acad Sci U S A 90:11257–11261 .

https://doi.org/10.1073/pnas.90.23.11257

Mandel AM, Akke M, Palmer AG (1995) Backbone dynamics of Escherichia coli ribonuclease HI: Correlations with structure and function in an active enzyme. J Mol Biol 246:144–163 . https://doi.org/10.1006/jmbi.1994.0073

Mielke S, Krishnan V (2009) Characterization of protein secondary structure from NMR chemical shifts. Prog Nucl Magn Reson Spectrosc 54:141–165 . https://doi.org/10.1016/b978-1-4832-2943-0.50008-x

Morin S, Gagné SM (2009) NMR dynamics of PSE-4 β-lactamase: An interplay of ps-ns order and μs-ms motions in the active site. Biophys J 96:4681–4691 . https://doi.org/10.1016/j.bpj.2009.02.068

Ortega A, Amoros D, Garcia de la Torre J (2011) Prediction of Hydrodynamic and Other Solution Properties of Rigid Proteins from Atomic- and Residue-Level Models. 101:892–898 . https://doi.org/10.1016/j.bpj.2011.06.046

Pastor N, Amero C (2015) Information flow and protein dynamics: the interplay between nuclear magnetic resonance spectroscopy and molecular dynamics simulations. Front Plant Sci 6:1–13 . https://doi.org/10.3389/fpls.2015.00306

Patel MP, Hu L, Stojanoski V, Sankaran B, Prasad BVV, Palzkill T (2017) The Drug-Resistant Variant P167S Expands the Substrate Profile of CTX-M β-Lactamases for Oxyimino-Cephalosporin Antibiotics by Enlarging the Active Site upon Acylation. Biochemistry 56:3443–3453 . https://doi.org/10.1021/acs.biochem.7b00176

Pemberton OA, Noor RE, Vasantha Kumar M V., Sanishvili R, Trent Kemp M, Kearns FL, Lee Woodcock H, Gelis I, Chen Y (2020) Mechanism of proton transfer in class A β-lactamase catalysis and inhibition by avibactam. Proc Natl Acad Sci U S A 117:5818–5825 . https://doi.org/10.1073/pnas.1922203117

Petrosino JF, Palzkill T (1996) Systematic Mutagenesis of the Active Site Omega Loop of TEM-I β-Lactamase. J Bacteriol 178:1821–1828 . https://doi.org/10.1128/jb.178.7.1821-1828.1996

Petrovic D, Risso VA, Kamerlin SCL, Sanchez-Ruiz JM (2018) Conformational dynamics and enzyme evolution. J R Soc Interface 15: . https://doi.org/10.1098/rsif.2018.0330

Pettersen EF, Goddard TD, Huang CC, Couch GS, Greenblatt DM, Meng EC, Ferrin TE (2004) UCSF Chimera - A Visualization System for Exploratory Research and Analysis. J Comput Chem 25:1605–1612 . https://doi.org/10.1002/jcc.20084

Phillips JC, Braun R, Wang W, Gumbart J, Tajkhorshid E, Villa E, Chipot C, Skeel RD, Kalé L, Schulten K (2005) Scalable Molecular Dynamics with NAMD. J Comput Chem 26:1781–1802 . https://doi.org/10.1002/jcc.20289

Riek R, Pervushin K, Wüthrich K (2000) TROSY and CRINEPT: NMR with large molecular and supramolecular structures in solution. Trends Biochem Sci 25:462–468 . https://doi.org/10.1016/S0968-0004(00)01665-0

Ryckaert JP, Ciccotti G, Berendsen HJC (1977) Numerical integration of the Cartesian Equations of Motion of a System with Constraints: Molecular Dynamics of n-Alkanes. J Comput Phys 23:327–341 . https://doi.org/10.1016/0021-9991(77)90098-5

Savard PY, Gagné SM (2006) Backbone dynamics of TEM-1 determined by NMR: Evidence for a highly ordered protein. Biochemistry 45:11414–11424 . https://doi.org/10.1021/bi060414q

Schumann FH, Riepl H, Maurer T, Gronwald W, Neidig KP, Kalbitzer HR (2007) Combined chemical shift changes and amino acid specific chemical shift mapping of protein-protein interactions. J Biomol NMR 39:275–289 . https://doi.org/10.1007/s10858-007-9197-z

Shen Y, Bax A (2013) Protein backbone and sidechain torsion angles predicted from NMR chemical shifts using artificial neural networks. J Biomol NMR 56:227–241 . https://doi.org/10.1007/s10858-013-9741-y

Shimamura T, Ibuka A, Fushinobu S, Wakagi T, Ishiguro M, Ishii Y, Matsuzaw H (2002) Acyl-intermediate structures of the Extended-spectrum Class A β-lactamase, Toho-1, in Complex with Cefotaxime, Cephalothin,

and Benzylpenicillin. J Biol Chem 277:46601–46608 . https://doi.org/10.1074/jbc.M207884200

Shimamura T, Nitanai Y, Uchiyama T, Matsuzawa H (2009) Improvement of crystal quality by surface mutations of beta-lactamase Toho-1 crystallization communications. Acta Crystallogr Sect F Struct Biol Cryst Commun F65:379–382 . https://doi.org/10.1107/S1744309109008240

Shimizu A, Ikeguchi M, Sugai S (1994) Appropriateness of DSS and TSP as internal references for 1H NMR studies of molten globule proteins in aqueous media. J Biomol NMR 4:859–862 . https://doi.org/10.1007/BF00398414

Shin J, Lee W, Weontae L (2006) Structural proteomics by NMR spectroscopy. Proteomics 5:171–185 . https://doi.org/10.1002/0470007745.ch9

Shirley M (2018) Ceftazidime-Avibactam: A Review in the Treatment of Serious Gram-Negative Bacterial Infections. Drugs 78:675–692 . https://doi.org/10.1007/s40265-018-0902-x

Skinner SP, Fogh RH, Boucher W, Ragan TJ, Mureddu LG, Vuister GW (2016) CcpNmr AnalysisAssign: a flexible platform for integrated NMR analysis. J Biomol NMR 66:111–124 . https://doi.org/10.1007/s10858-016-0060-y

Spyracopoulos L (2006) A suite of Mathematica notebooks for the analysis of protein main chain 15N NMR relaxation data. J Biomol NMR 36:215–224 . https://doi.org/10.1007/s10858-006-9083-0

Stojanoski V, Chow DC, Hu L, Sankaran B, Gilbert HF, Prasad BVV, Palzkill T (2015) A Triple Mutant in the Ω-loop of TEM-1 β-Lactamase Changes the Substrate Profile via a Large Conformational Change and an Altered General Base for Catalysis. J Biol Chem 290:10382–10394 . https://doi.org/10.1074/jbc.M114.633438

Tjandra N, Feller SE, Pastor RW, Bax A (1995) Rotational Diffusion Anisotropy of Human Ubiquitin from 15N NMR Relaxation. J Am Chem Soc 117:12562–12566 . https://doi.org/10.1021/ja00155a020

Tollinger M, Skrynnikov NR, Mulder FAA, Forman-Kay JD, Kay LE (2001) Slow Dynamics in Folded and Unfolded States of an SH3 Domain. J Am Chem Soc 123:11341–11352 . https://doi.org/10.1021/ja011300z

Tomanicek SJ, Blakeley MP, Cooper J, Chen Y, Afonine P V., Coates L (2010) Neutron Diffraction Studies of a Class A β-lactamase Toho-1 E166A/R274N/R276N Triple Mutant. J Mol Biol 396:1070–1080 . https://doi.org/10.1016/j.jmb.2009.12.036

Tomanicek SJ, Standaert RF, Weiss KL, Ostermann A, Schrader TE, Ng JD, Coates L (2013) Neutron and X-ray Crystal Structures of a Perdeuterated Enzyme Inhibitor Complex Reveal the Catalytic Proton Network of the Toho-1 β-Lactamase for the Acylation Reaction. J Biol Chem 288:4715–4722 . https://doi.org/10.1074/jbc.M112.436238

Tooke CL, Hinchliffe P, Bragginton EC, Colenso CK, Hirvonen VHA, Takebayashi Y, Spencer J (2019) β-Lactamases and β-Lactamase Inhibitors in the 21st Century. J Mol Biol 431:3472–3500 . https://doi.org/10.1016/j.jmb.2019.04.002

Vandavasi VG, Weiss KL, Cooper JB, Erskine PT, Tomanicek SJ, Ostermann A, Schrader TE, Ginell SL, Coates L (2016) Exploring the Mechanism of β-Lactam Ring Protonation in the Class A β-lactamase Acylation Mechanism Using Neutron and X-ray Crystallography. J Med Chem 59:474–479 . https://doi.org/10.1021/acs.jmedchem.5b01215

Verma D, Jacobs DJ, Livesay DR (2013) Variations within Class-A β-Lactamase Physiochemical Properties Reflect Evolutionary and Environmental Patterns, but not Antibiotic Specificity. PLOS Comput Biol 9: . https://doi.org/10.1371/journal.pcbi.1003155

Wang L, Eghbalnia HR, Bahrami A, Markley JL (2005) Linear analysis of carbon-13 chemical shift differences and its application to the detection and correction of errors in referencing and spin system identifications. J Biomol NMR 32:13–22 . https://doi.org/10.1007/s10858-005-1717-0

Williamson MP (2013) Using chemical shift perturbation to characterise ligand binding. Prog Nucl Magn Reson Spectrosc 73:1–16 . https://doi.org/10.1016/j.pnmrs.2013.02.001

Woessner DE (1962) Nuclear spin relaxation in ellipsoids undergoing rotational brownian motion. J Chem Phys 37:647–654 . https://doi.org/10.1063/1.1701390

Zou T, Risso VA, Gavira JA, Sanchez-Ruiz JM, Ozkan SB (2015) Evolution of Conformational Dynamics Determines the Conversion of a Promiscuous Generalist into a Specialist Enzyme. Mol Biol Evol 32:132–143 . https://doi.org/10.1093/molbev/msu281